Hillslope recovery after a major earthquake: InSAR-derived time series analyses to capture earthquake-legacy effect

Kun He[1,2], Luigi Lombardo[2], Ling Chang[2], Nitheshnirmal Sadhasivam[2], Xiewen Hu[1], Zhice Fang[2,3], Ashok Dahal[2], Islam Fadel[2], Gang Luo[1], Hakan Tanyas*[2]

[1]Southwest Jiaotong University, Faculty of Geosciences and Environmental Engineering, Chengdu, China

[2]University of Twente, Faculty of Geo-Information Science and Earth Observation (ITC), Enschede, Netherlands

[3]China University of Geosciences, Institute of Geophysics and Geomatics, Wuhan, China

*Corresponding Author: Hakan Tanyas (h.tanyas@utwente.nl)

Abstract

Mountainous landscapes affected by strong earthquakes exhibit relatively higher landslide susceptibility in post-seismic periods compared to pre-seismic conditions. This concept is referred to as the earthquake legacy effect and is mainly examined by monitoring either rapid landslide occurrences or slow-moving landslides over time. To provide a more comprehensive understanding of the concept, this research examines post-seismic hillslope evolution by examining the deformation time series generated by the Interferometric Synthetic Aperture Radar technique over the entirety of the area affected by the 2017 M_w 6.4 Nyingchi, China earthquake. Our results show that the average post-seismic hillslope deformation level in the study area is still higher than its pre-seismic counterpart approximately four and a half years after the earthquake. Our findings trigger further research questions regarding whether hillslopes could fully recover after a major earthquake or gain a new level of hillslope susceptibility caused by intense ground shaking.

1. Introduction

Landslides pose serious threats to communities, especially in mountainous regions such as the Himalayan range where thousands of lives and billions of Euros are lost every year because of landslides (Upreti et al., 2001). For these mountainous communities, earthquakes are a common triggering factor for landslides, causing disastrous cascading effects (e.g., Roback et al., 2018; Sato et al., 2007).

Seismic shaking is not only responsible for co-seismic landslides -- the main secondary earthquake hazard (Daniell et al., 2017) -- but can also be the reason for some long-term hillslope instability problems because of the intrinsic damage given to hillslope materials (e.g., Chen et al., 2020; Parker et al., 2015). In post-seismic periods, the earthquake legacy effect couples with climatic/anthropogenic disturbances and exacerbates hillslope instabilities (Kincey et al., 2021). Some argue that the landscape returns to pre-seismic landslide susceptibility level only after months or even years, depending on site-specific morphologic and climatic conditions typical of the area (e.g., Tian et al. 2020).

The process that any given landscape naturally undergoes to be restored to its pre-seismic slope stability conditions is commonly referred to as hillslope recovery. And, this recovery is mostly assessed through multi-temporal landslide inventories including various types of landslides including both shallow and deep-seated ones (Tanyaş et al., 2021a). Specifically, pre- and post- landslide susceptibility levels are commonly identified on the basis of the frequency of landslide occurrence and the results are interpreted to infer the hillslope evolution processes in earthquake-affected areas. However, focusing on only landslide occurrences limits our observations with a small subset of the landscape under consideration. Shear strength perturbation could occur on any hillslopes affected by seismic shaking, regardless of whether a landslide would end up manifesting or not (Tanyaş et al., 2021b). This also means that relatively higher hillslope deformation rates could be considered as a sign of relatively higher landslide susceptibility (i.e., the relative probability of landslide occurrence) compared to hillslopes with lower deformation rates.

To provide a more comprehensive picture of landscape evolution, Interferometric Synthetic Aperture Radar (InSAR) is also used to monitor post-seismic hillslope transformation (e.g., Bontemps et al., 2020; Lacroix et al., 2022). In this case, hillslope observations are not bounded by landslide occurrences but by continuous slope movements, albeit being restricted to particularly slow ones. Our assumption here is that hillslope recovery analyses could be significantly enriched if observations are extended beyond failed hillslopes, encompassing even slight deformations (i.e., milliner level) that take place over the entirety of seismically-perturbed landscapes. InSAR can play a crucial role in monitoring such slight deformation rates over large areas at longer time spans by examining the pre- and post- seismic periods and excluding the co-seismic period that could be associated with rapid moving landsides that may not be captured by InSAR observations. Following this hypothesis, here we examine hillslope deformation (HD) over the area affected by the 2017 Nyingchi earthquake in the time span between 1.5 years before the event to 4.5 years after which was intervened by subsequent three 5.0 Mw earthquakes in 2019, 2020 and 2021. In doing so, we generate InSAR-derived HD for pre- and post-seismic periods, excluding the co-seismic periods to minimize the effect of the associated rapidly moving landslides.

The remainder of the manuscript will present our study site (Section 2), methodology (Section 3), and results (Section 4), which emphasize the sudden increase in HD associated with the Nyingchi earthquake and a post-seismic overall landscape response where the HD still appears higher than its pre-seismic expression even after four and a half years from the mainshock. In Section 5, we discuss our interpretation and share our concluding remarks.

2. Study area and data

We examined an area located on the western edge of the Himalayan range (Fig. 1). This area was shaken on the 17th of November 2017, by the M_w 6.4 Nyingchi, China earthquake as well as its three large aftershocks (of magnitude greater or equal to 5.0) in the following month (USGS, 2022). The resulting effect on slope instabilities has already been described by Zhao et al. (2019), with more than 1,800 landslides being mapped over a 530 km^2

area (depicted by the black points in Fig. 1). After this seismic sequence, the same area was also hit by three subsequent earthquakes of magnitude 5.0 in 2019, 2020 and 2021 (Fig. 1).

This study thus focuses on a particularly complex system where the aforementioned earthquake sequence shook a rough mountainous landscape (80km x 95km) where changes in elevation reach up to ~7 km in a relatively short distance. Despite the high mountainous system, the land surface temperature is above zero from March to December, and glacier bodies exclusively persist only across the high peaks (Fig. 1). In this overall terrain description, human intervention has limited influence, with land cover types been mainly expressed by natural forest, grassland and barelands, and only a few patches being dedicated to agricultural practices (ESA Climate Change Initiative, 2022).

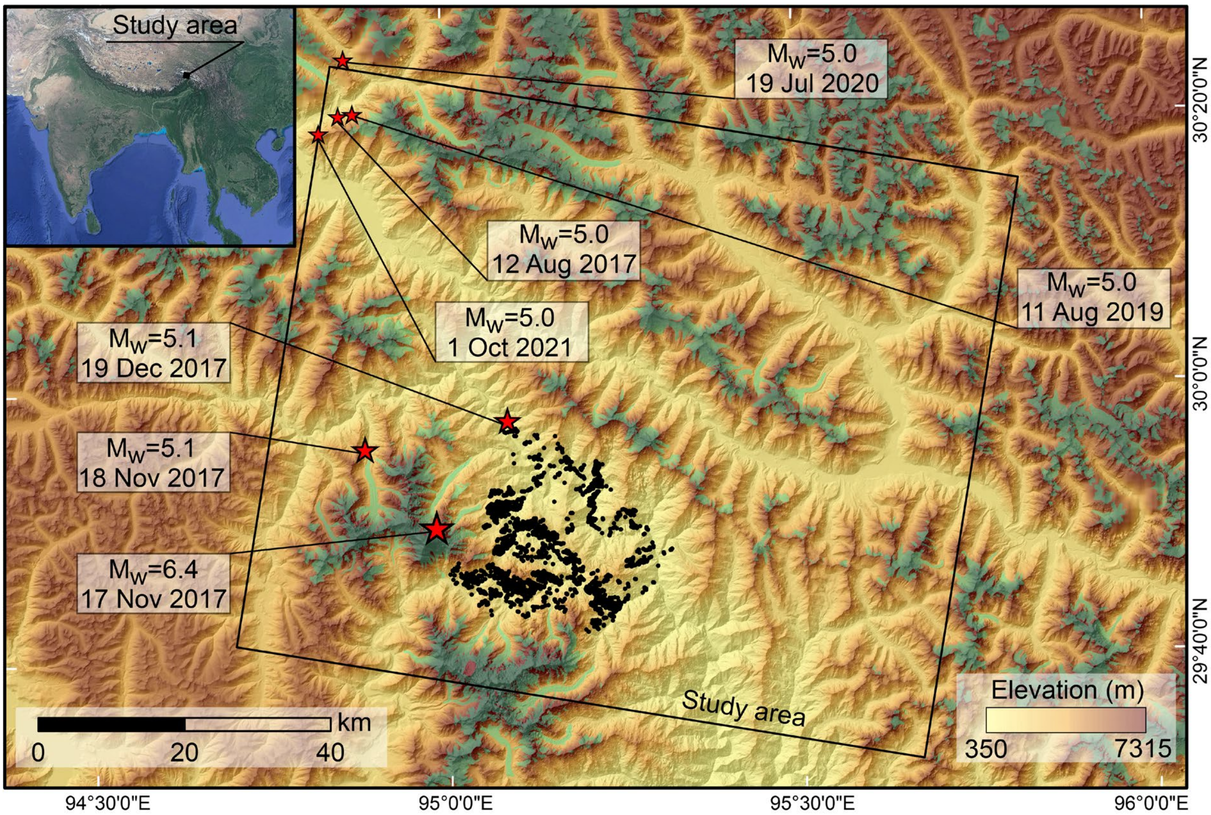

Figure 1. The study area overlaid by epicenters of earthquakes that occurred in the last five years (USGS, 2022) and landslides triggered by the 2017, M_w 6.4 Nyingchi earthquake (Zhao et al., 2019) are depicted by black points. Glaciers (GLIMS Consortium, 2005; Raup et al., 2007) are indicated by green polygons.

To look at factors potentially influencing HD, we examined InSAR-derived surface displacements in relation to climatic variables, including precipitation (The Global Precipitation Measurement, GPM - Integrated Multi-satellite Retrievals, IMERG final product; Huffman et al. 2019) and terrestrial water storage (TWS, Li et al. 2019, 2020). TWS is a dataset (0.25° spatial resolution and 1-day temporal resolution) mainly generated from the Gravity and Recovery and Climate Experiment satellites and it indicates the water storage as the sum of various factors including soil moisture, groundwater, surface waters, snow and ice, canopy interception and wet biomass (Li et al., 2019). This means that precipitation is one of the variables contributing to TWS.

For InSAR time series analyses, we used 147 C-Band Sentinel-1 satellite SAR images acquired between May 2016 and July 2022, in VV polarization channel. For the study area, Sentinel-1 ascending data is not available and thus, we collected data in descending orbital direction, with path 4 and frame 491 (Table 1), which cover the area affected by the 2017 Nyingchi earthquake region (outlined by the black square in Fig. 1).

Table 1. Sentinel-1 data used in the analyses

Time Stacks (TSs)	Satellite	Sentinel-1 (SLC)
	Orbit	Descending
	Beam	IW
	Path	4
	Frame	491
	Polarization	VV
	Heading angle (degree)	190
	Incidence angle (degree)	36.76~42.43
TS1 (Pre-seismic)	Acquisition dates	15.05.2016~18.11.2017
	Number of scenes	25
TS2 (Post-seismic)	Acquisition dates	30.11.2017~30.04.2019
	Number of scenes	40
TS3 (Post-seismic)	Acquisition dates	16.08.2019~17.07.2020
	Number of scenes	24
TS4 (Post-seismic)	Acquisition dates	29.07.2020~22.09.2021
	Number of scenes	35
TS5 (Post-seismic)	Acquisition dates	04.10.2021~25.06.2022
	Number of scenes	23

3. Method

We applied Persistent Scatterer Interferometry (PSI) to identify HD (Ferretti et al., 2001). Specifically, we split the examined time window into five-time stacks (TSs) with an average length of a year (Table 1). We used earthquake occurrence dates as a reference to determine the TSs. As a result, this not only helps us to analyse pre- and post- seismic periods separately but also to examine shorter sequential time stacks where coherence between acquisitions could be preserved to generate more Persistent Scatterer (PS) points separately during these five-time intervals.

The SNAP, SNAP2StaMPS and StaMPS software packages were used for the implementation of interferometric and time series analysis (Delgado Blasco et al., 2019; Foumelis et al., 2018; Hooper et al., 2018, 2012), with atmospheric correction conducted using the Generic Atmospheric Correction Online Service (GACOS) product

(Yu et al. 2018). The master images are selected per TS in a way that we have a shortest possible temporal baseline between all the available images, which also helps in maintaining the coherence between master and slave images (Crosetto et al., 2016). Then we removed the topographic and the flattened earth phases using the SRTM DEM (30m) and applied 3D phase unwrapping to generate PS deformation time series estimation in line of sight (LOS) direction. We assume that the effect of the atmospheric phase on the deformation measurements is minimized by applying the GACOS product. Since the study area is affected by a sequence of earthquakes and owing to the unavailability of a known stable point, the value for the reference point is taken from the average value of all PSI points present in the entire region (Hooper et al., 2012). Details of the InSAR analyses are provided in the Supplementary Materials.

As a result of InSAR analyses, slow deformations in both upward and downward directions could be captured. In the context of hillslope deformations associated with landsliding, PS displacements pointing out uphill movements could be discarded in the analyses (e.g., Herrera et al. 2013). However, differentiating HD with a downslope component from the rest is not a straightforward task. Notably, the PSI technique provides deformations in LOS directions as well as average annual velocities (V_{LOS}). Based on the relative position of hillslopes with respect to the heading angle of the satellite (α, 190º for our case), V_{LOS} could exhibit positive or negative signs (Colesanti and Wasowski, 2006; Notti et al., 2014). On the one hand, downslope deformations on hillslopes facing toward the SAR sensor take positive values. On the other hand, downslope HD on hillslopes facing away from the sensor is identified with negative values. Because this research aims at identifying HD, we categorized PS points with positive or negative V_{LOS} with different aspect values and only focused on the ones with downslope deformation components. More specifically, we followed three steps (Fig. 2). First, we masked flat areas (slope<10°, e.g., Kritikos et al., 2015) to filter out deformation which may not be associated with hillslopes. To identify the threshold value of slope steepness, we performed visual checks to ensure that the majority of flood planes with gentle slopes were removed from the analyses. Second, we categorized the PS points into classes. Class (i) contains the PS points with an aspect facing towards to sensor (i.e., (α-180, α]) and Class (ii) includes the ones with an aspect away from the sensor (i.e., (α, α-180]). Ultimately, the PS points with positive V_{LOS} from class (i) and negative ones from class (ii) were selected and combined. In the rest of the analyses, we took their absolute values and only used these PS points.

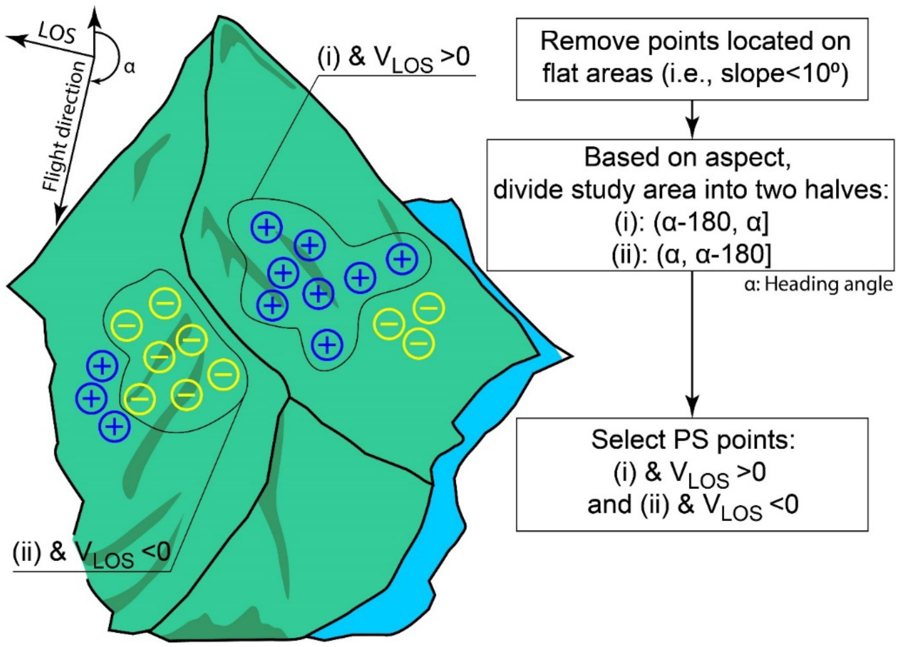

Figure 2. Schematic drawing showing the methodology applied to identify HD along the downslope component.

To visualize these HD systematically through the study area, we aggregated V_{LOS} for each hillslope following Sadhasivam (2022). There, we used the *r.slopeunits* software (Alvioli et al., 2016) to delineate landscape partitions, called slope units (SUs). These are characterized by similar aspect values and are mainly bounded by ridges between adjacent hillslopes.

To examine the link between climatic variables (precipitation and TWS) and surface deformation, we used Cross Wavelet Transform (XWT, Grinsted et al. 2004). XWT examines time-frequency domains and identifies the corresponding sections of time series carrying large common power with a consistent phase relationship to determine the coherence between examined datasets. To perform this analysis, we also applied spline interpolation to our deformation time series to generate equally-spaced time intervals (i.e., 12 days) where we can consistently compare the deformation time series with climatic variables (e.g., Schlögl et al., 2021; Tomás et al., 2016).

4. Results

We generated PS points from pre-seismic (TS1) to post-seismic (TS2-TS5) phases (Fig. 3). There are 391354, 171926, 400294, 394225, and 429418 PS points in total for TS1, TS2, TS3, TS4 and TS5, respectively. Overall, in the study area, V_{LOS} values vary between -100 and 100 mm/year. The pre-seismic (TS1) shows the velocity of LOS spanning from -31 to 33 mm/year, which is lower than, for instance, the LOS rate of -50 mm to 50 mm/year observed in the pre-Gorkha earthquake period in the Himalayas (Bekaert et al., 2020). Between the five time stacks, TS2 represents the one right after the 2017 M_w 6.4 Nyingchi earthquake. In fact, TS2 is also the time window with the lowest PS point density. Post-seismic landsliding rates from the literature could explain the reason behind this low-density PS point distribution. The first few months right after a large seismic shock generally refer to a period where landsliding rates are still elevated compared to pre-seismic conditions (Tanyaş et al., 2021a). Therefore, the coherence loss associated with large post-seismic hillslope failures, which can't be captured using PSI technique could be the reason for low-density PS point distribution.

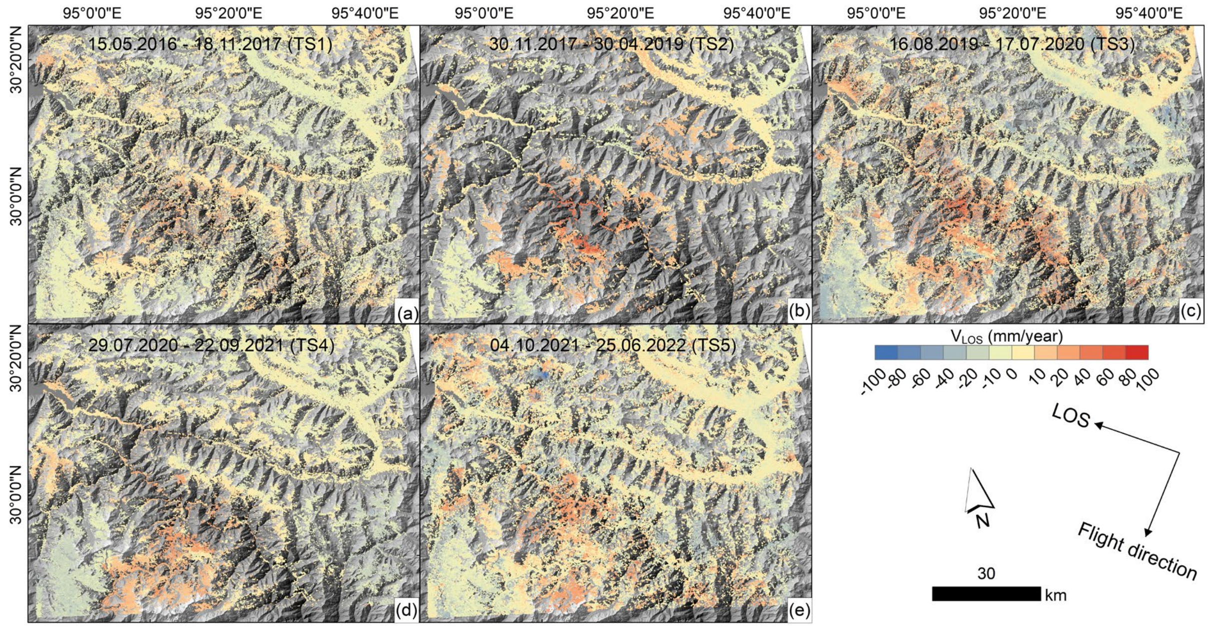

Figure 3. Spatial distribution of PS points from pre-seismic (a) to post-seismic (b-e) periods.

The row PS points and associated V_{LOS} values presented in Figure 3 were filtered out to extract only the HD with downslope components (see Method section). After aggregating absolute values of V_{LOS} for SUs, we visualized hillslopes with only downslope deformations, which are color-coded as a function of the mean average annual V_{LOS} in Figures 4a-4e. Post-seismic evolution of hillslope displacements shows a rapid increase in deformations right after the 2017 Nyingchi earthquake, during TS2. Specifically, the mean average annual V_{LOS} reaches up to 50 mm/year in this time stack. Figure 4f also shows the same elevated deformation values over the entirety of the study area. In the majority of SU, the variation in HD shows an increasing trend from TS1 to TS2. Overall, deformations in TS3 are still higher than in TS1 but with a slight decrease compared to TS2 (Fig. 4g). In fact, from TS3 onwards, the elevated HD noticed in TS2 begins to fade away. And, although deformations are overall still above the pre-seismic conditions, they are not as high as TS2.

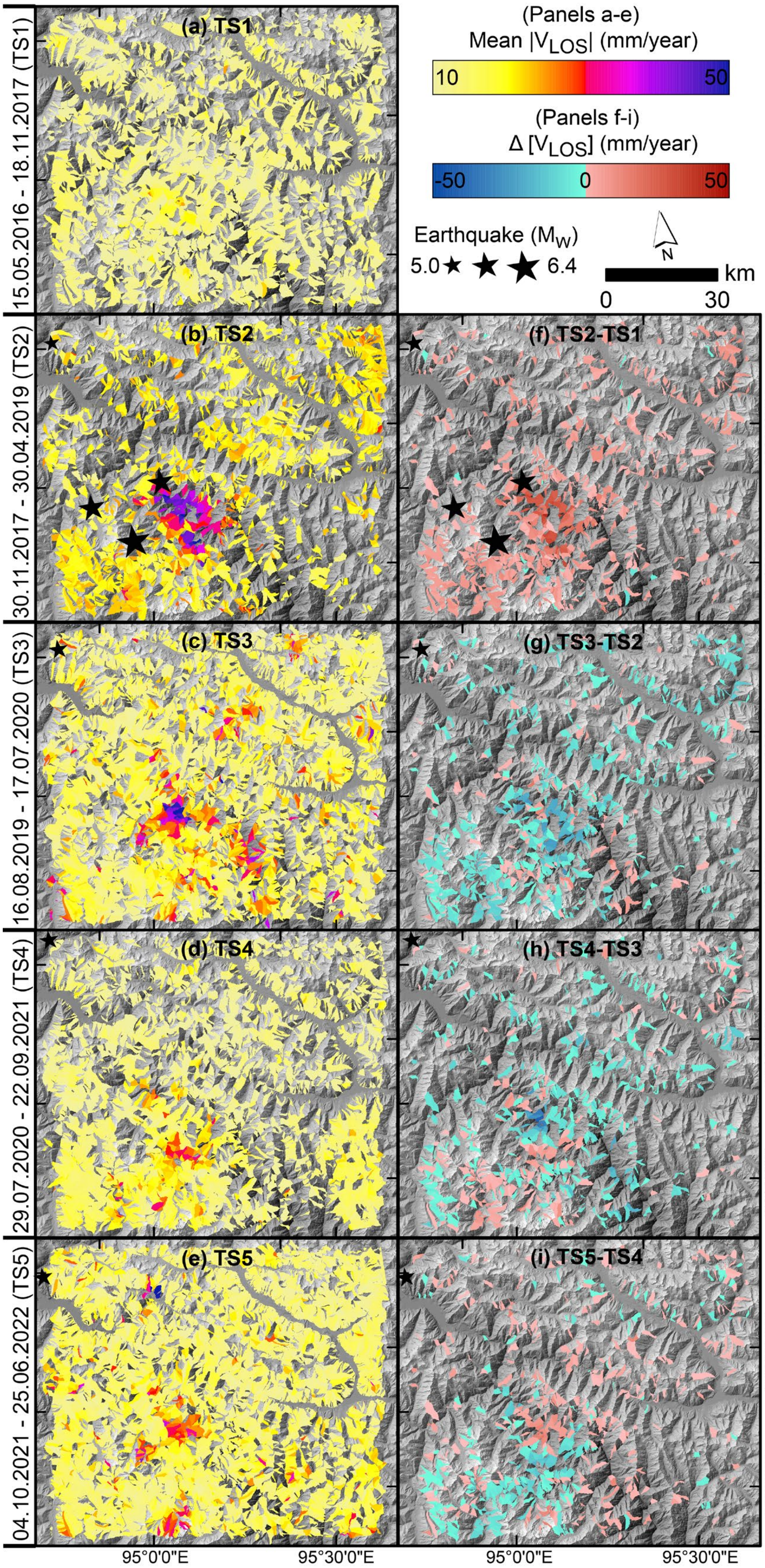

Figure 4. Evolution of HD from pre- to post- seismic periods. Panels from (a) to (e) show mean average V_{LOS} from TS1 to TS5, respectively. Panels (f-i) indicate the difference in V_{LOS} between each successive time stuck, namely Δ [V_{LOS}].

Another observation is that the spatial distribution of HD only matches with the epicentral locations of the 2017 M_w 6.4 Nyingchi earthquake and its nearby aftershocks (Fig. 4b). However, from TS3 to TS5, other earthquakes of M_w 5.0 (see the north-western corner of the study area in Fig. 4) do not show any ground motion pattern that could be visibly linked to that of the estimated HD. We should stress that this is not conclusive evidence given the limited observation at the border of the study area. On the contrary, relatively high deformations still concentrate around the epicentre of the Nyingchi earthquake (Figs. 4c-4e). This shows that from TS2 to TS5, the overall post-seismic HD is mainly derived from the legacy effect of the 2017 Nyingchi earthquake.

We univariately summarized the same information in Figure 5, by expressing the mean average V_{LOS} for each time stack from TS1 to TS5. Results also show a statistically significant increase in hillslope deformations right after the main earthquake and then, a gentle decreasing trend up to TS5. For instance, the respective HD median values are 11.7, 20.4, 15.9, 14.2 and 14.0 from TS1 to TS5. This shows that post-seismic HD are still higher than the pre-seismic level. This also implies that approximately four and a half years after the earthquake, the earthquake legacy effect still influences hillslope deformations and its signature has yet to fade away. Regardless of the presence of any slow-moving landslides, its influence is still detectable as part of seasonal hillslope deformations.

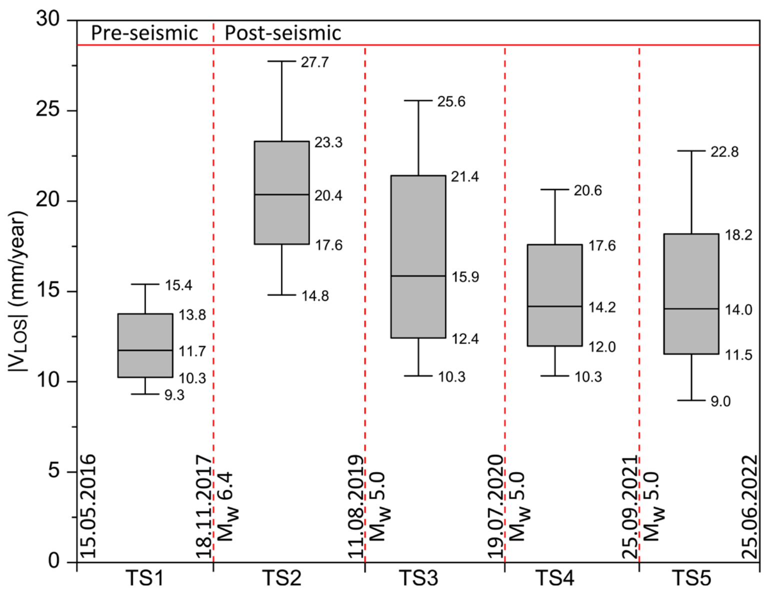

Figure 5. Evolution of mean average V_{LOS} from TS1 to TS5. Outliers were removed from the analyses.

We also examined hillslope evolution using deformation time series instead of V_{LOS}. To carry out this analysis for the whole study area, we calculated mean deformation values and compared them with respect to precipitation and TWS. The visual comparison shows that TWS is high in wet seasons as one can expect (Fig. 6a and 6b). Because the study area receives most of its precipitation in these seasons, TWS is high in these periods and deformations appear to be high as well. This is to highlight that hillslopes demonstrate a seasonal deformation pattern in TS1, TS3, TS4 and TS5. Nevertheless, right after the 2017 Nyingchi earthquake in TS2, the correlation between both climatic proxies and HD seems to be negative (Fig. 6a and 6b).

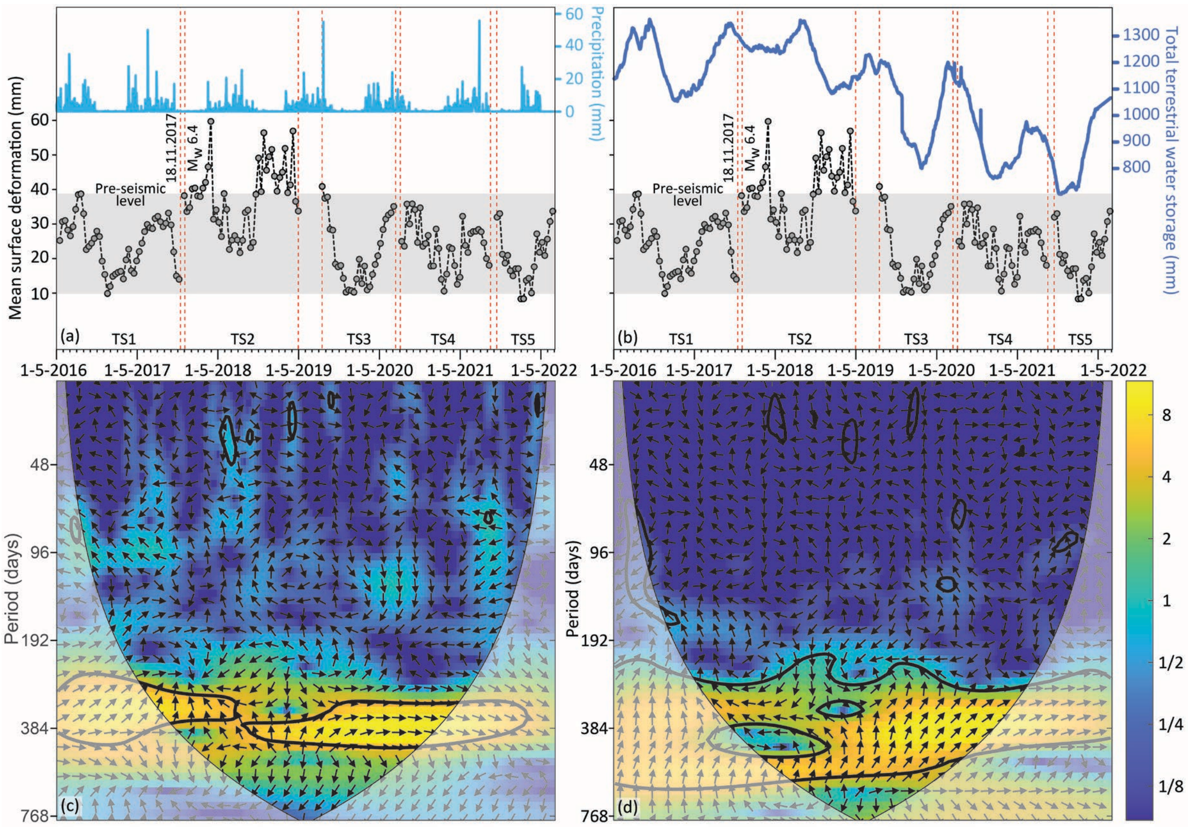

Figure 6. Panels showing variation in hillslope deformation (HD) time series in relation to (a) precipitation and (b) total terrestrial water storage (TWS). Panels (c) and (d) show cross wavelet transforms (XWT) of precipitation and HD as well as TWS and HD, respectively. In panels (a) and (b) the grey-shaded areas indicate the range of pre-seismic HD. In panels (c) and (d) color pallet from blue to yellow indicates increasing similarities between common patterns in the examined time series. The 5% significance level against red noise is indicated by the black contour lines and the cone of influence where edge effects might distort the picture is shown as a lighter shade (Grinsted et al., 2004).

To numerically examine the correlation, we used XWTs of precipitation and HD (Fig. 6c) as well as TWS and HD (Fig. 6d). Results show a significant coherence between the time series (i.e., common features in the wavelet power of the two time series) in both cases with approximately one year period (see black polygons in Fig. 6c and 6d), though, TS2 shows lack of coherence as well as slightly different period and phase. Arrows indicate the phase difference (i.e., the lag time) between time series. Overall, arrows pointing to the right indicates positive correlation and arrows pointing left represent negative correlation. XWT of precipitation and HD shows arrows pointing out upper right; ~45° from the horizontal axis in the pre-seismic period, which indicates approximately 45 days (1/8 of a cycle) lag-time between precipitation and HD (Fig. 6c). Also, arrows pointing out right in the post-seismic periods (i.e., TS3-TS5) show a strong in-phase correlation indicating that precipitation and HD are coincidental in the post-seismic periods (Fig. 6c). A similar observation is also valid for the XWT of TWS and HD (Fig. 6d). From pre-seismic to post-seismic periods, the lag time between TWS and HD gradually decreases, and in TS5 the two time series becomes almost coincidental in time. Notably, precipitation gives a relatively shorter lag time compared to TWS because the former one refers to a process feeding the latter one with a lag time.

Results indicate a strong correlation with varying time lags between the two time series except for TS2. There, HD still might be connected to climatic variables, but they do not appear as the ones dominating the overall deformation. Also, some local variations, for instance, the water table fluctuation, might not be well represented in this global dataset of TWS. Notably, strong earthquakes could cause changes in groundwater level and its recovery may take several hours to several months depending on tectonic and lithological conditions (Liu et al., 2018).

5. Discussion and Conclusions

This research focuses on the evolution of post-seismic HD, a concept mostly studied using exclusively the visible deformation recorded in multi-temporal landslide inventories or in a number of targeted slow-moving landslides. Conversely, the novel contribution in this work is the use of InSAR-derived HD to study earthquake legacies. Specifically, we consistently examine the whole HD in the area affected by the 2017 Nyingchi earthquake. Our results show that average V_{LOS} values are still higher than the pre-seismic period, approximately four and a half years after the earthquake. Despite this observation, it also appears evident that V_{LOS} values are following a decreasing trend, which implies that the earthquake legacy effect has still been nullifying (see Fig. 5).

However, when we focus on the deformation time series, the pre-seismic deformation level seems to be reached in TS3, approximately two years after the Nyingchi earthquake (see Fig. 6a). There, a discussion point should be raised to further investigate whether this recovery in hillslopes is fully associated with the earthquake legacy effect or if some other external factors may play a role in this recovery. For instance, if the hillslopes received less precipitation in the post-seismic periods compared to its pre-seismic counterpart, this might have also caused relatively smaller hillslope deformation in the post-seismic period. In fact, the decreasing HD trend shown from TS3 onwards largely matched the decreasing trend in TWS during the same period. For this reason, the apparent recovery of the HD to pre-seismic levels could be dependent on a lower water content rather than on processes of hillslope recovery.

Testing this hypothesis requires decoupling the water content signal from the HD one, because minimizing the climatic contribution could provide a better and less biased insight into post-seismic hillslope evolution processes. To accomplish this task, we used TSW, which is a variable representing the delayed effect of precipitation on hillslopes. We initially standardized both TWS and HD time series subtracting their respective means and dividing each time point by their respective standard deviation. This procedure, commonly referred to as mean-zero, unit-variance ensures that both time series are rescaled to the same unitless range (Fig. 7a). In a second step, acknowledging that HD should be better analysed by minimizing the influence of the TWS signal, we normalized once more both time series, anchoring their respective intra-seismic distributions to the pre-seismic one. In other words, we calculated the mean TWS values for each time stack and shifted the TWS time series in TS2, TS3, TS4 and TS5 to the level shown in TS1. We also applied the same shifts in the corresponding HD time series, for TS2, TS3, TS4 and TS5 (Fig. 7a). Results show the HD time series normalized as a function of TWS, for each time stack. By decreasing the contribution of the hillslope water storage, we observe that HDs are still higher than the pre-seismic level, something we observed in the raw HD data plotted in Figure 5. This also implies that the earthquake legacy effect still influences HD approximately even four and a half years after the earthquake.

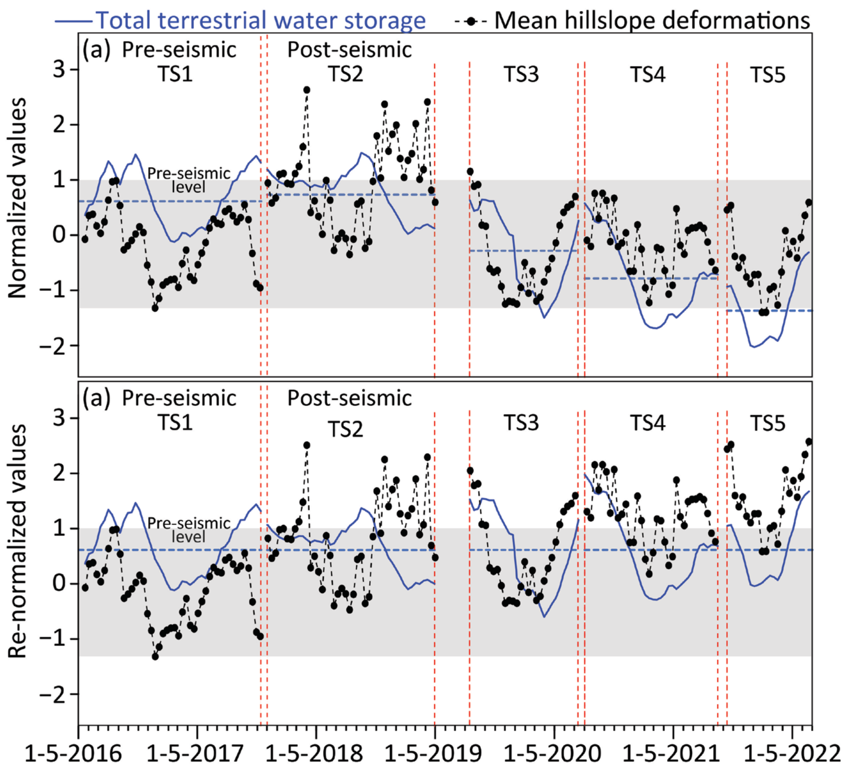

Figure 7. Time series of total terrestrial water storage (TWS) and mean hillslope deformations (HD) after (a) mean-zero and unit-variance normalization and (b) re-normalization of HD with respect to TWS in pre-seismic phase. The grey-shaded area indicates the range of pre-seismic HD.

We should stress once more that the hillslope recovery time we mention here is not comparable to the landslide recovery time often discussed in the literature where authors exploited discrete landslide information over time to assess it (e.g., Tang et al. 2016; Fan et al. 2018; Kincey et al. 2021). In this context, examples of landslide recovery could be plausible for periods longer than four and half years only for a few cases corresponding to quite strong earthquakes, such as 1999 M_w 7.7 Chi-Chi, 2005 M_w 7.6 Kashmir, 2008 M_w 7.9 Wenchuan or 2015 M_w 7.8 Gorkha (Tanyaş et al., 2021a). However, this consideration cannot be easily generalized for the number of observations we can rely upon is very limited. For instance, even among the very few long-term studies, significant differences do exist. In some exceptional cases, authors hypothesize persisting earthquake legacies over multiple decades whereas in other situations this is confined within a few years. The former example corresponds to Parker et al. (2015), as they argue that the legacy effect of the 1929 M_w 7.7 Buller earthquake still persists in the landslide distribution associated with the 1968 M_w 7.1 Inangahua earthquake. Aside from the specific example at hand, the most generic argument is that higher HD should be associated with higher landslide susceptibility/hazard. In this context, the landslide recovery time identified from landslide inventories might not reflect the actual post-seismic hillslope conditions because not all the ground motion disturbance translates into an actual failure. Slopes that were on the brink of instability certainly may have a higher chance to fail, but it is also true that slopes that were previously stable may be brought close to failure without it actually manifesting. This is the reason why exclusively focusing on landslide inventories for the estimation of recovery times may largely underestimate or at least provide strongly biased information related to the earthquake legacy effect on hillslope stability. This discussion points out some further research questions that still need to be addressed. Specifically, the link between hillslope recovery and landslide susceptibility/hazard should require further analysis to numerically express how the variation in hillslope recovery influences landslide susceptibility level. Furthermore, a more robust identification of post-seismic hillslope strength could also help us improve landslide susceptibility and hazard assessment after strong earthquakes.

Acknowledgments

We are very grateful to Alessandro Cesare Mondini for providing valuable feedback to improve the quality of this manuscript. The Geospatial Computing Platform of the Center of Expertise in Big Geodata Science (CRIB) (https://crib.utwente.nl) is used for the processing of Sentinel-1 data. We thank Dr. Serkan Girgin for his support in providing the necessary computing infrastructure.

Data availability

All data used in this research was collected from publicly available data sources.

Author contribution

HT conceptualised the research idea. InSAR analyses were carried out by KH, LC, NS and HT. HT, LL and KH wrote the manuscript whereas LC, NS, XH, ZF, IF, AD and GL provided feedback on it.

Competing interests

The authors declare no competing interest.

References

Alvioli, M., Marchesini, I., Reichenbach, P., Rossi, M., Ardizzone, F., Fiorucci, F., Guzzetti, F., 2016. Automatic delineation of geomorphological slope units with r.slopeunits v1.0 and their optimization for landslide susceptibility modeling. Geosci. Model Dev. 9, 3975–3991. https://doi.org/10.5194/gmd-9-3975-2016

Bekaert, D.P.S., Handwerger, A.L., Agram, P., Kirschbaum, D.B., 2020. InSAR-based detection method for mapping and monitoring slow-moving landslides in remote regions with steep and mountainous terrain: An application to Nepal. Remote Sens. Environ. 249, 111983. https://doi.org/https://doi.org/10.1016/j.rse.2020.111983

Bontemps, N., Lacroix, P., Larose, E., Jara, J., Taipe, E., 2020. Rain and small earthquakes maintain a slow-moving landslide in a persistent critical state. Nat. Commun. 11, 1–10. https://doi.org/10.1038/s41467-020-14445-3

Chen, M., Tang, C., Xiong, J., Shi, Q.Y., Li, N., Gong, L.F., Wang, X.D., Tie, Y., 2020. The long-term evolution of landslide activity near the epicentral area of the 2008 Wenchuan earthquake in China. Geomorphology 367, 107317. https://doi.org/https://doi.org/10.1016/j.geomorph.2020.107317

Colesanti, C., Wasowski, J., 2006. Investigating landslides with space-borne Synthetic Aperture Radar (SAR) interferometry. Eng. Geol. 88, 173–199. https://doi.org/https://doi.org/10.1016/j.enggeo.2006.09.013

Crosetto, M., Monserrat, O., Cuevas-González, M., Devanthéry, N., Crippa, B., 2016. Persistent Scatterer Interferometry: A review. ISPRS J. Photogramm. Remote Sens. 115, 78–89.

https://doi.org/https://doi.org/10.1016/j.isprsjprs.2015.10.011

Daniell, J.E., Schaefer, A.M., Wenzel, F., 2017. Losses associated with secondary effects in earthquakes. Front. Built Environ. 3, 1–14. https://doi.org/10.3389/fbuil.2017.00030

Delgado Blasco, J.M., Foumelis, M., Stewart, C., Hooper, A., 2019. Measuring Urban Subsidence in the Rome Metropolitan Area (Italy) with Sentinel-1 SNAP-StaMPS Persistent Scatterer Interferometry. Remote Sens. . https://doi.org/10.3390/rs11020129

ESA Climate Change Initiative, 2022. Land Cover - led by UCLouvain. “2015 global land cover.” Accessed through Global Forest Watch on 09/11/2022. www.globalforestwatch.org [WWW Document].

Fan, X., Domènech, G., Scaringi, G., Huang, R., Xu, Q., Hales, T.C., Dai, L., Yang, Q., Francis, O., 2018. Spatio-temporal evolution of mass wasting after the 2008 Mw 7.9 Wenchuan earthquake revealed by a detailed multi-temporal inventory. Landslides 15, 2325–2341. https://doi.org/10.1007/s10346-018-1054-5

Ferretti, A., Prati, C., Rocca, F., 2001. Permanent scatterers in SAR interferometry. IEEE Trans. Geosci. Remote Sens. 39, 8–20. https://doi.org/10.1109/36.898661

Foumelis, M., Blasco, J.M.D., Desnos, Y., Engdahl, M., Fernandez, D., Veci, L., Lu, J., Wong, C., 2018. Esa Snap - Stamps Integrated Processing for Sentinel-1 Persistent Scatterer Interferometry, in: IGARSS 2018 - 2018 IEEE International Geoscience and Remote Sensing Symposium. pp. 1364–1367. https://doi.org/10.1109/IGARSS.2018.8519545

GLIMS Consortium, 2005. GLIMS Glacier Database, Version 1 [Data Set]. Boulder, Colorado USA. NASA National Snow and Ice Data Center Distributed Active Archive Center. https://doi.org/10.7265/N5V98602. Date Accessed 11-09-2022 [WWW Document].

Grinsted, A., Moore, J.C., Jevrejeva, S., 2004. Application of the cross wavelet transform and wavelet coherence to geophysical time series. Nonlin. Process. Geophys. 11, 561–566. https://doi.org/10.5194/npg-11-561-2004

Herrera, G., Gutiérrez, F., García-Davalillo, J.C., Guerrero, J., Notti, D., Galve, J.P., Fernández-Merodo, J.A., Cooksley, G., 2013. Multi-sensor advanced DInSAR monitoring of very slow landslides: The Tena Valley case study (Central Spanish Pyrenees). Remote Sens. Environ. 128, 31–43. https://doi.org/https://doi.org/10.1016/j.rse.2012.09.020

Hooper, A., Bekaert, D., Ekbal, H., Spaans, K., 2018. StaMPS/MTI manual: Version 4.1 b. Sch. Earth Environ. Univ. Leeds. Retrieved Oct. 15, 2019.

Hooper, A., Bekaert, D., Spaans, K., Arikan, M., 2012. Recent advances in SAR interferometry time series analysis for measuring crustal deformation. Tectonophysics 514–517, 1–13. https://doi.org/10.1016/j.tecto.2011.10.013

Huffman, G., Stocker, E.F., T, B.D., Nelkin, E.J., Tan, J., 2019. GPM IMERG Final Precipitation L3 1 day 0.1 degree x 0.1 degree V06 [WWW Document]. Ed. by Andrey Savtchenko, Greenbelt, MD, Goddard Earth Sci. Data Inf. Serv. Cent. (GES DISC). https://doi.org/10.5067/GPM/IMERGDF/DAY/06

Kincey, M.E., Rosser, N.J., Robinson, T.R., Densmore, A.L., Shrestha, R., Pujara, D.S., Oven, K.J., Williams, J.G., Swirad, Z.M., 2021. Evolution of coseismic and post-seismic landsliding after the 2015 Mw 7.8 Gorkha earthquake, Nepal. J. Geophys. Res. Earth Surf. n/a, e2020JF005803. https://doi.org/https://doi.org/10.1029/2020JF005803

Kritikos, T., Robinson, T.R., Davies, T.R.H., 2015. Regional coseismic landslide hazard assessment without historical landslide inventories: A new approach. J. Geophys. Res. Earth Surf. 120, 711–729. https://doi.org/10.1002/2014JF003224

Lacroix, P., Gavillon, T., Bouchant, C., Lavé, J., Mugnier, J.-L., Dhungel, S., Vernier, F., 2022. SAR and optical images correlation illuminates post-seismic landslide motion after the Mw 7.8 Gorkha earthquake (Nepal). Sci. Rep. 12, 6266. https://doi.org/10.1038/s41598-022-10016-2

Li, B., Beaudoing, H., Rodell, M., 2020. GLDAS Catchment Land Surface Model L4 daily 0.25 x 0.25 degree GRACE-DA1 V2.2, Greenbelt, Maryland, USA, Goddard Earth Sciences Data and Information Services Center (GES DISC), Accessed: 9.11.22 [WWW Document]. https://doi.org/10.5067/TXBMLX370XX8

Li, B., Rodell, M., Kumar, S., Beaudoing, H.K., Getirana, A., Zaitchik, B.F., de Goncalves, L.G., Cossetin, C., Bhanja, S., Mukherjee, A., Tian, S., Tangdamrongsub, N., Long, D., Nanteza, J., Lee, J., Policelli, F., Goni, I.B., Daira, D., Bila, M., de Lannoy, G., Mocko, D., Steele-Dunne, S.C., Save, H., Bettadpur, S., 2019. Global GRACE Data Assimilation for Groundwater and Drought Monitoring: Advances and Challenges. Water Resour. Res. 55, 7564–7586. https://doi.org/https://doi.org/10.1029/2018WR024618

Liu, C.-Y., Chia, Y., Chuang, P.-Y., Chiu, Y.-C., Tseng, T.-L., 2018. Impacts of hydrogeological characteristics on groundwater-level changes induced by earthquakes. Hydrogeol. J. 26, 451–465.

https://doi.org/10.1007/s10040-017-1684-z

Notti, D., Herrera, G., Bianchini, S., Meisina, C., García-Davalillo, J.C., Zucca, F., 2014. A methodology for improving landslide PSI data analysis. Int. J. Remote Sens. 35, 2186–2214. https://doi.org/10.1080/01431161.2014.889864

Parker, R.N., Hancox, G.T., Petley, D.N., Massey, C.I., Densmore, A.L., Rosser, N.J., 2015. Spatial distributions of earthquake-induced landslides and hillslope preconditioning in the northwest South Island, New Zealand. Earth Surf. Dyn. 3, 501–525. https://doi.org/10.5194/esurf-3-501-2015

Raup, B., Racoviteanu, A., Khalsa, S.J.S., Helm, C., Armstrong, R., Arnaud, Y., 2007. The GLIMS geospatial glacier database: a new tool for studying glacier change. Glob. Planet. Change 56, 101–110. https://doi.org/10.1016/j.gloplacha.2006.07.018

Roback, K., Clark, M.K., West, A.J., Zekkos, D., Li, G., Gallen, S.F., Chamlagain, D., Godt, J.W., 2018. The size, distribution, and mobility of landslides caused by the 2015 Mw7.8 Gorkha earthquake, Nepal. Geomorphology 301, 121–138. https://doi.org/10.1016/j.geomorph.2017.01.030

Sadhasivam, N., 2022. Unveiling earthquake legacy effects on hillslopes using InSAR. University of Twente.

Sato, H.P., Hasegawa, H., Fujiwara, S., Tobita, M., Koarai, M., Une, H., Iwahashi, J., 2007. Interpretation of landslide distribution triggered by the 2005 Northern Pakistan earthquake using SPOT 5 imagery. Landslides 4, 113–122. https://doi.org/10.1007/s10346-006-0069-5

Schlögl, M., Widhalm, B., Avian, M., 2021. Comprehensive time-series analysis of bridge deformation using differential satellite radar interferometry based on Sentinel-1. ISPRS J. Photogramm. Remote Sens. 172, 132–146. https://doi.org/https://doi.org/10.1016/j.isprsjprs.2020.12.001

Tang, C., Van Westen, C.J., Tanyas, H., Jetten, V.G., 2016. Analysing post-earthquake landslide activity using multi-temporal landslide inventories near the epicentral area of the 2008 Wenchuan earthquake. Nat. Hazards Earth Syst. Sci. 16. https://doi.org/10.5194/nhess-16-2641-2016

Tanyaş, H., Kirschbaum, D., Görüm, T., van Westen, C.J., Tang, C., Lombardo, L., 2021a. A closer look at factors governing landslide recovery time in post-seismic periods. Geomorphology 391, 107912. https://doi.org/https://doi.org/10.1016/j.geomorph.2021.107912

Tanyaş, H., Kirschbaum, D., Lombardo, L., 2021b. Capturing the footprints of ground motion in the spatial distribution of rainfall-induced landslides. Bull. Eng. Geol. Environ. https://doi.org/10.1007/s10064-021-02238-x

Tian, Y., Owen, L.A., Xu, C., Ma, S., Li, K., Xu, X., Figueiredo, P.M., Kang, W., Guo, P., Wang, S., Liang, X., Maharjan, S.B., 2020. Landslide development within 3 years after the 2015 Mw 7.8 Gorkha earthquake, Nepal. Landslides 17, 1251–1267. https://doi.org/10.1007/s10346-020-01366-x

Tomás, R., Li, Z., Lopez-Sanchez, J.M., Liu, P., Singleton, A., 2016. Using wavelet tools to analyse seasonal variations from InSAR time-series data: a case study of the Huangtupo landslide. Landslides 13, 437–450. https://doi.org/10.1007/s10346-015-0589-y

Upreti, B.N., N, B., Chalise, R, S., Tianchi, L, 2001. Landslide Hazard Mitigation in the Hindu Kush-Himalayas. International Centre for Integrated Mountain Development (ICIMOD). https://doi.org/10.53055/ICIMOD.374

USGS, 2022. United States geological survey earthquake portal. Earthquake Hazards Program [WWW Document]. URL https://www.usgs.gov/%0Anatural-hazards/earthquake-hazards/earthquakes (accessed 4.27.21).

Zhao, B., Li, W., Wang, Y., Lu, J., Li, X., 2019. Landslides triggered by the Ms 6.9 Nyingchi earthquake, China (18 November 2017): analysis of the spatial distribution and occurrence factors. Landslides 16, 765–776. https://doi.org/10.1007/s10346-019-01146-2